日本磁気学会
ISSN 2432-0250
Journal of the Magnetics Society of Japan
Electronic Journal URL: https://www.jstage.jst.go.jp/browse/msjmag

Vol.49 No.2　2025

Journal

Hard and Soft Magnetic Materials

Magnetic Anisotropy of Sm(Fe-Co-Ni)$_{12}$-B Thin Films and Formation of ThMn$_{12}$ Phase by Element Substitution and Addition

Y. Mori, S. Nakatsuka, T. Sato, M. Doi, and T. Shima　…27

Power Magnetics

Characteristics of PMSM with $Sm_2Fe_{17}N_3/Fe_{16}N_2$ Hybrid Bonded Magnets

İ. Çirozlar, S. Murakami, K. Nakamura, T. Ogawa, S. Yamamoto, N. Kobayashi, and H. Yamamoto　…32

JOURNAL OF THE MAGNETICS SOCIETY OF JAPAN

Vol.49 No.2 2025

日本磁気学会

ISSN 2432-0250

HP: http://www.magnetics.jp/ e-mail: msj@bj.wakwak.com

Electronic Journal: http://www.jstage.jst.go.jp/browse/msjmag

TOEI

TPM-2-08s25

HcJの3σ/Ave. 0.2%[※1]を実現

渦電流補正方法[※2]も確立済

試料測定磁界
max 15Tesla

最大試料直径
10mm

パルス励磁型磁気特性測定装置

永久磁石および磁性体粉末を固形化した高磁化試料のヒステリシス曲線の自動測定および描画、SPD（Singuler Point Detection）測定が可能です。（RT～+200℃）

※1　電気学会資料 MAG-18-088 参照

※2　電気学会資料 MAG-07-011 参照

NdFeB(sintered) 測定例

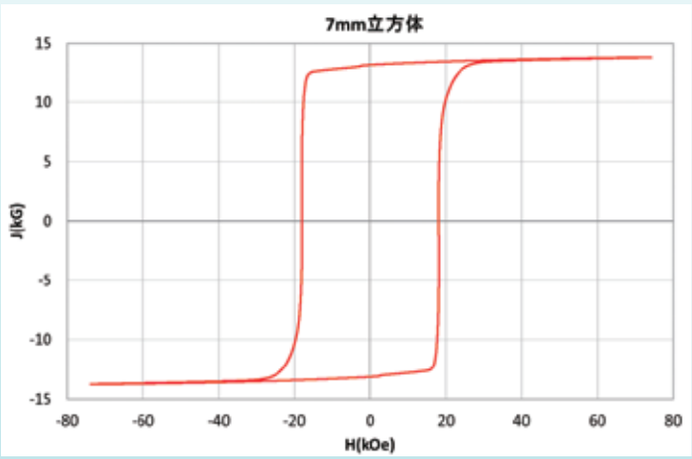

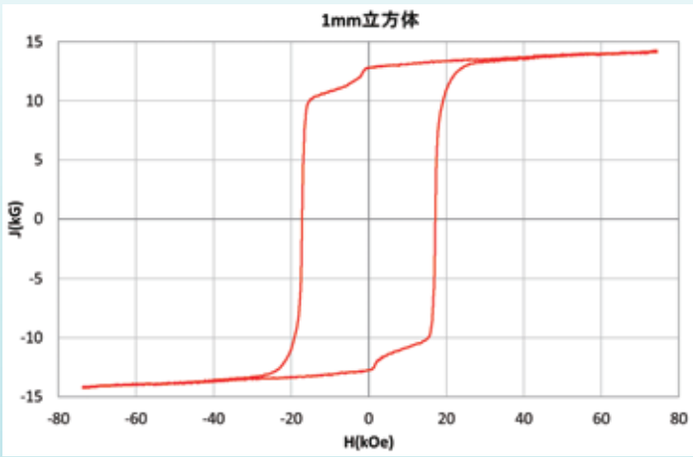

1mm 立方体測定用検出コイルはオプション品です

東英工業では他に振動試料型磁力計(VSM)、直流自記磁束計(JIS C2501 準拠)を始め、

各種磁気測定装置を取り揃えております。ぜひお問い合わせ下さい

TOEI 東英工業株式会社
http://www.toeikogyo.co.jp

〒194-0035 東京都町田市忠生1-8-13
TEL：042-791-1211 FAX：042-792-0490
E-mail：sales@toeikogyo.co.jp

Journal of the Magnetics Society of Japan
Vol. 49, No. 2

Electronic Journal URL: https://www.jstage.jst.go.jp/browse/msjmag

CONTENTS

Hard and Soft Magnetic Materials

Magnetic Anisotropy of Sm(Fe-Co-Ni)$_{12}$-B Thin Films and Formation of ThMn$_{12}$ Phase by Element Substitution and Addition
..... Y. Mori, S. Nakatsuka, T. Sato, M. Doi, and T. Shima 27

Power Magnetics

Characteristics of PMSM with $Sm_2Fe_{17}N_3/Fe_{16}N_2$ Hybrid Bonded Magnets
..... İ. Çirozlar, S. Murakami, K. Nakamura, T. Ogawa, S. Yamamoto, N. Kobayashi, and H. Yamamoto 32

J. Magn. Soc. Jpn., **49**, 27-31 (2025) <Paper>

Magnetic anisotropy of $Sm(Fe\text{-}Co\text{-}Ni)_{12}$-B thin films and formation of $ThMn_{12}$ phase by element substitution and addition

Y. Mori*†, S. Nakatsuka*, T. Sato**, M. Doi*, and T. Shima*
*Graduate School of Engineering, Tohoku Gakuin Univ., *Shimizukoji* , *Sendai 984-8588, Japan*
**Faculty of Engineering, Tohoku Gakuin Univ., *Shimizukoji* , *Sendai 984-8588, Japan*

The combined addition of Ni and Co is a promising method for stabilizing the $ThMn_{12}$-type crystal structure without significantly decreasing the saturation magnetization. In this work, the structure and magnetic properties of $Sm(Fe\text{-}Co)_{12}$-B thin films by substituting Ni and Co with a part of Fe sites and adding B were investigated in detail. It was observed that when the Fe sites of $Sm(Fe\text{-}Co\text{-}Ni)_{12}$ thin films were partially substituted with Ni, the peak intensity from the $ThMn_{12}$-type phase decreased, but recovered with increasing the amount of Co substitution. Furthermore, most of the samples with combined Ni and Co substitution had an isotropic or in-plane easy axis of magnetization with respect to the film plane. However, it was confirmed that the easy axis of magnetization was varied to the perpendicular direction by adding a small amount of B to the $Sm(Fe\text{-}Co\text{-}Ni)_{12}$ thin films.

Keywords: $ThMn_{12}$-type crystal structure, magnetic anisotropy, element substitution, $Sm(Fe\text{-}Co\text{-}Ni)_{12}$-B thin film

1. Introduction

RFe_{12} (R: rare earth element) compounds (hereafter referred to as 1:12) with a tetragonal $ThMn_{12}$-type crystal structure are expected to have a high saturation magnetization due to their high Fe content, and they are promising candidates for new high-performance permanent magnet materials. In particular, it has been confirmed that $SmFe_{12}$-based compounds exhibit superior intrinsic magnetic properties at room temperature and at high temperatures compared with $Nd_2Fe_{14}B$ sintered magnets[1)-6)]. For example, the saturation magnetization ($\mu_0 M_s$ = 1.78 T), anisotropy field ($\mu_0 H_A$ = 12 T), and Curie temperature (T_C = 879 K) can be obtained at room temperature in a $Sm(Fe_{0.8}Co_{0.2})_{12}$ thin film[1)]. Furthermore, it was reported that a high coercive force of 1.2 T was obtained in a B-doped Sm(Fe-Co)-B thin film prepared by sputtering, which is due to a columnar structure in which $Sm(Fe\text{-}Co)_{12}$ particles were surrounded by the grain boundary phase[7)]. In recent years, we have succeeded in further increasing the coercivity of $Sm(Fe\text{-}Co)_{12}$-B thin films through the grain boundary diffusion of nonmagnetic elements[8)-11)], and we reported that a particularly large coercivity ($\mu_0 H_c$ = 1.8 T) can be obtained by depositing an Al cap layer[11)]. However, in previous studies, it was well known that the $SmFe_{12}$ phase was thermodynamically unstable in the bulk state, and therefore it was necessary to substitute some of the Fe sites with stabilizing elements such as Al, Si, Ti, V, Co, and Zr[12)-14)]. The addition of these stabilizing elements inevitably results in a significant decrease in the saturation magnetization of the $SmFe_{12}$ compound, which has been a major drawback. Therefore, in order to obtain a sufficiently high saturation magnetization while maintaining the stability of $ThMn_{12}$-type compounds, it is necessary to either minimize the amount of stabilizing elements added or to replace part of the Fe sites with ferromagnetic elements that function as stabilizers.

Recently, Landa et al. reported using a fundamental framework based on density-functional theory in which $SmNi_4(Fe\text{-}Co)_8$ alloys exhibit a negative formation energy and that the formation energy is minimal when the mole fraction of Co in Fe-Co is 0.4[15)-16)]. To obtain a high saturation magnetization without affecting the

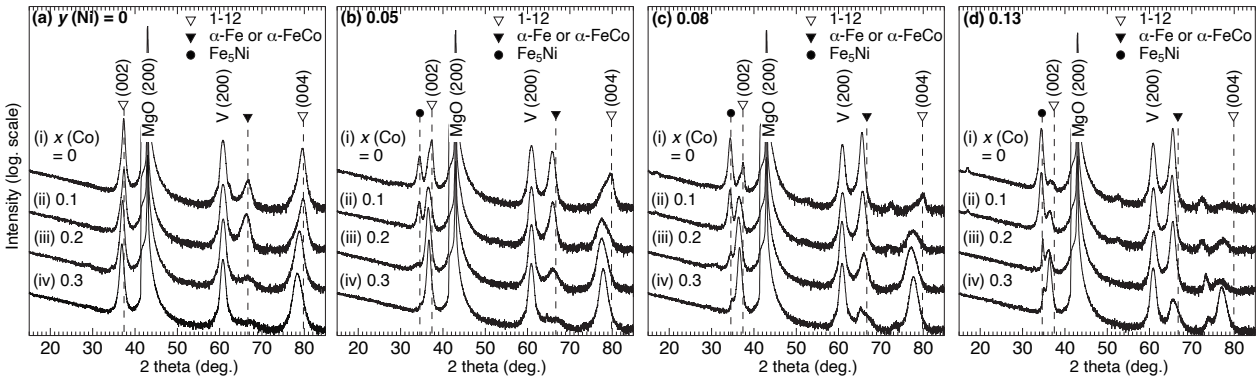

Fig. 1. Out-of-plane XRD patterns for $Sm(Fe_{1-x-y}Co_xNi_y)_{12}$ thin films with different amount of Ni substitution [(a) ~ (d)] and Co substitution [(i) ~ (iv)].

Corresponding author: Y. Mori (e-mail: s236532001@g.tohoku-gakuin.ac.jp).

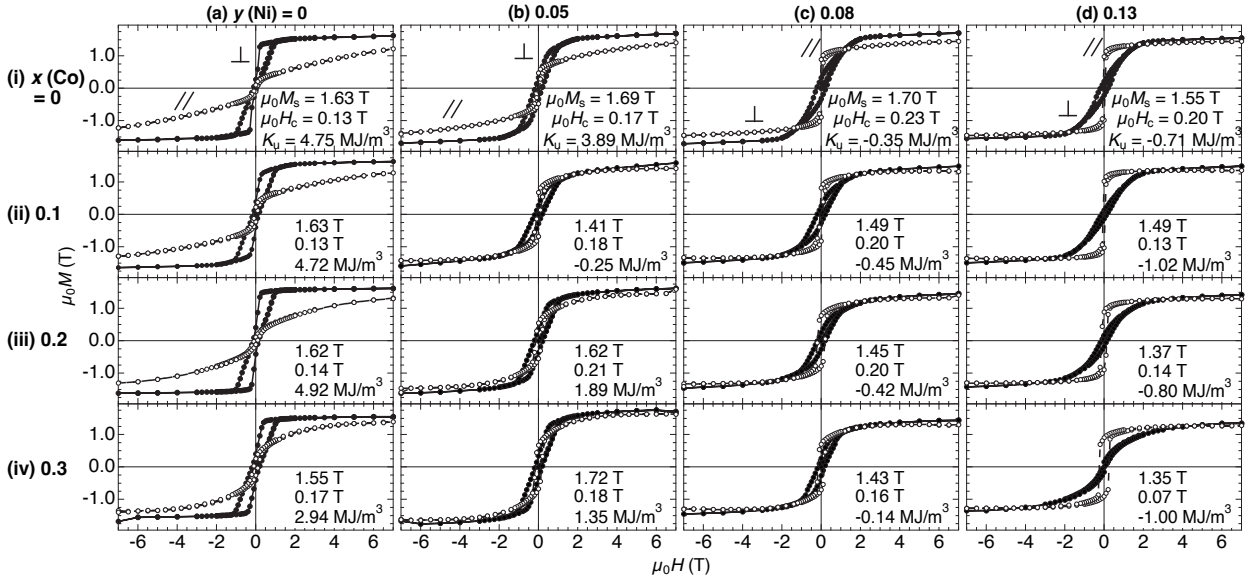

Fig. 2. Magnetization curves for $Sm(Fe_{1-x-y}Co_xNi_y)_{12}$ [x: (i) ~ (iv), y: (a) ~ (d)] thin films. Filled and open circles are denoted curves measured in perpendicular and parallel directions to the film plane, respectively.

anisotropy field or Curie temperature, they propose replacing a certain amount of Fe and Co with Ni in $Sm(Fe_{1-x}Co_x)_{12}$ alloys. Therefore, the simultaneous substitution of Ni and Co is expected to be a candidate method for stabilizing the $SmFe_{12}$ phase without significantly decreasing the saturation magnetization. In this study, $Sm(Fe\text{-}Co)_{12}$ and $Sm(Fe\text{-}Co)_{12}$-B thin films with added Ni, which is expected to stabilize the $ThMn_{12}$-type phase without significantly decreasing saturation magnetization, are prepared and the crystal structure and magnetic properties by variation of the film composition, such as the amount of Co and Ni substituted for Fe and the amount of B added are also investigated in detail.

2. Experimental procedure

The samples were prepared by using an ultra-high vacuum magnetron sputtering system with an ultimate pressure of less than 4.0×10^{-7} Pa. First, a V buffer layer with a thickness of 20 nm was deposited on a MgO(100) single crystal substrate at a substrate temperature (T_s) of 400ºC in an Ar gas atmosphere with a process gas pressure of 0.17 Pa. Subsequently, a 50 nm of $Sm(Fe_{1-x-y}Co_xNi_y)_{12}$-B layer ($x$ = 0 ~ 0.5, y = 0 ~ 0.13) was deposited by co-sputtering with Sm, Fe, $Fe_{50}Co_{50}$, $Fe_{80}B_{20}$ and Ni targets at T_s = 400ºC. The mole fractions of Ni and Co (x, y) were determined from the results of energy dispersive X-ray analysis (EDX). However, due to the detection limit of light elements, the content of B cannot be determined by EDX, so the B content was determined by the ratio of the deposition rate of boron to that of the $Sm(Fe\text{-}Co\text{-}Ni)_{12}$-B layer. Finally, a 10-nm V cover layer was deposited as a protective layer to prevent oxidation at room temperature. The crystal structure was analyzed by X-ray diffraction (XRD) with Cu-K_α radiation by adjusting the χ and φ angles to adopt out-of-plane and in-plane configurations. The magnetic properties were evaluated using a superconducting quantum interference device (SQUID) magnetometer. All measurements were performed at room temperature.

3. Results and discussion

XRD patterns for $Sm(Fe_{1-x-y}Co_xNi_y)_{12}$ thin films with different amounts of Co substitution (x = 0 ~ 0.3) and Ni substitution (y = 0 ~ 0.13) are shown in Fig. 1. As shown in Fig. 1(a)(i), the (002) and (004) peaks of the $ThMn_{12}$-type crystal structure were clearly observed in the Ni- and Co-unsubstituted $SmFe_{12}$ thin film. At Co substitution x = 0.1, the position of the peak from the 1:12 phase remained almost unvaried, but it was confirmed that the peak position shifted to a lower angle with increasing x. It was confirmed that as the Ni substitution amount y increased from (a) to (d), the peak intensity from the 1:12 phase decreased, while at the same time, the peak intensities from the Fe_5Ni and α-Fe phases seen at 2θ = 34.6º and 66.6º increased. These results indicate that the substitution of Co into Fe sites elongates the lattice spacing of the c-plane, while the substitution of Ni inhibits the formation of the 1:12 phase and instead leads to the formation of Fe_5Ni and α-Fe phases. In addition, in the $Sm(Fe\text{-}Co\text{-}Ni)_{12}$ thin film [(b)-(d)], the peak intensity from the 1:12 phase was recovered by increasing the Co substitution amount x, and the peaks of the Fe_5Ni phase and the α-Fe phase were decreased, that is, their formation was suppressed. This suggests that the presence of Co facilitates the formation of the 1:12 phase with Ni added.

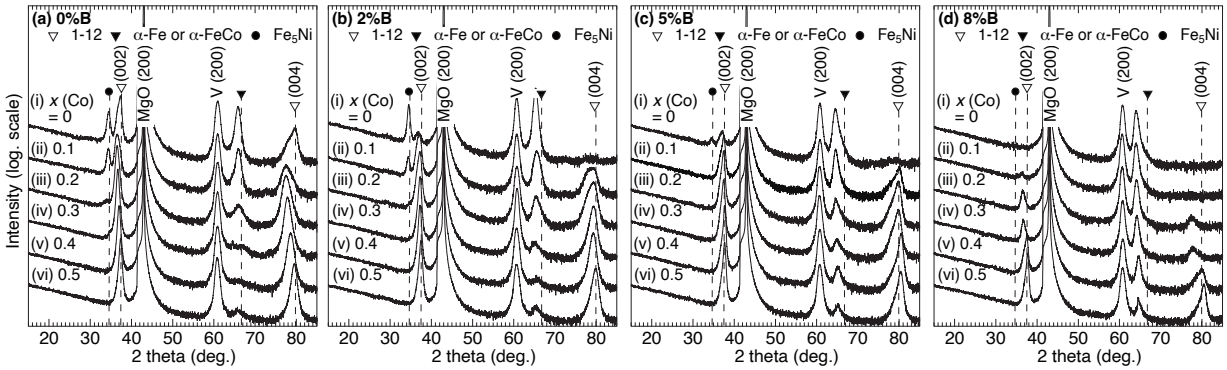

Fig. 3. XRD patterns for $Sm(Fe_{0.95-x}Co_xNi_{0.05})_{12}$-B thin films with different amount of B content [0 ~ 8% B: (a) ~ (d)] and Co substitution [x: (i) ~ vi)].

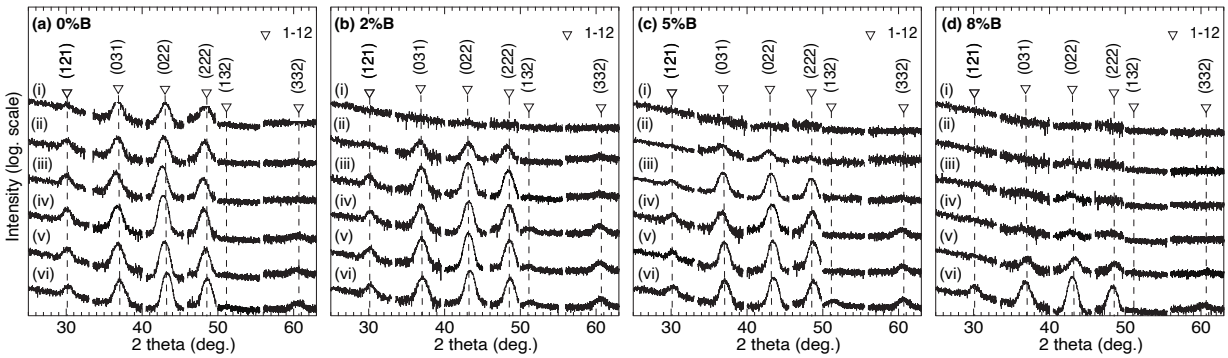

Fig. 4. In-plane XRD patterns for $Sm(Fe_{0.95-x}Co_xNi_{0.05})_{12}$-B thin films with different amount of B content [0 ~ 8% B: (a) ~ (d)] and Co substitution [x = 0 ~ 0.5: (i) ~ (vi)].

Magnetization curves for $Sm(Fe_{1-x-y}Co_xNi_y)_{12}$ thin films with different amounts of Co (x) and Ni (y) substitution are shown in Fig. 2. The filled and open circles denote the results measured in perpendicular and parallel directions to the film plane, respectively. In the $SmFe_{12}$ thin film without Co or Ni substitution (x = 0 and y = 0) shown in Fig. 2(a)(i), a high saturation magnetization $\mu_0 M_s$ =1.63 T exhibiting perpendicular magnetic anisotropy was obtained. Increasing the Co substitution amount x improved the squareness of the hysteresis loop in the first quadrant, but further increasing x to 0.3 decreased the uniaxial magnetic anisotropy constant (K_u). The value of K_u was calculated by subtracting the integral of the out-of-plane M-H curve from the integral of the in-plane M-H curve in the first quadrant. As shown in Fig. 2(b), when the Ni substitution amount y was 0.05, it was confirmed that K_u decreased due to Co substitution and the easy direction of magnetization varied from perpendicular to the film plane to almost isotropic. In addition, as shown in Fig. 2(c), when y was increased to 0.08, the easy axis of magnetization of the $Sm(Fe\text{-}Ni)_{12}$ thin film varied from the perpendicular direction to the film plane to the in-plane direction. Furthermore, even when the amounts of Co substitution and Ni substitution were further increased, the easy axis of magnetization remained in-plane. Thus, it was confirmed that Ni substitution does not contribute to improve the hard magnetic properties of $Sm(Fe\text{-}Co)_{12}$ compounds, and that the in-plane magnetic anisotropy becomes predominant as the Ni content increases. Therefore, an attempt was made to improve the anisotropy by adding B to $Sm(Fe\text{-}Co\text{-}Ni)_{12}$ thin films with a small amount of Ni substitution y = 0.05.

XRD patterns of $Sm(Fe_{0.95-x}Co_xNi_{0.05})_{12}$-B thin films prepared with different amounts of B content (B = 0 ~ 8%) and Co substitution (x = 0 ~ 0.5) measured in the out-of-plane configuration ($\chi = \varphi = 0$) are shown in Fig. 3. It should be noted that the B content is determined by the deposition rate of boron during the deposition of the $Sm(Fe_{0.95-x}Co_xNi_{0.05})_{12}$-B layer. In the B-free $Sm(Fe\text{-}Co\text{-}Ni_{0.05})$ thin film shown in Fig. 3(a), it was observed that the (002) and (004) peak positions of the 1:12 phase shifted to lower angles when x was 0.1, and then shifted to higher angles as x increased further. On the other hand, when the amount of B added was increased to 2% and 5%, the peak intensity of the 1:12 phase decreased in the case of samples not substituted with Co, and when the amount of B added was further increased to 8% (d), it was confirmed that the peak of the 1:12 phase almost completely disappeared. However, the peak intensity of the 1:12 phase was increased significantly in the 2%B and 5%B films by substituting Co into the Fe site (x = 0.1), and the peak intensity further increased with increasing x. In addition, it was confirmed that the peak intensity of the Fe_5Ni and α-Fe

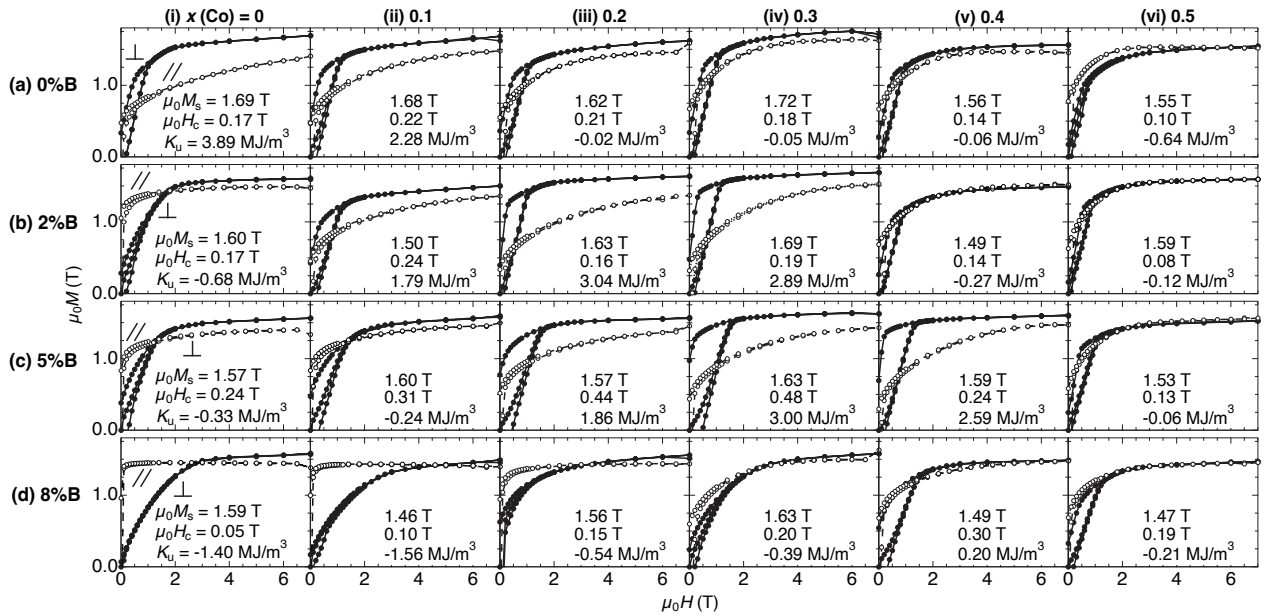

Fig. 5. Magnetization curves for $Sm(Fe_{0.95-x}Co_xNi_{0.05})_{12}$-B thin films with different amount of B content [0 ~ 8% B: (a) ~ (d)] and Co substitution [x: (i) ~ (vi)].

phases decreased with increasing Co substitution, suppressing their formation. In the 8%B sample, the peak intensity of the 1:12 phase recovered from 0.2 to 0.5 due to an increase in the Co substitution amount, but it was confirmed that the intensity was lower than that of the 5%B sample with a lower B addition at each x value.

XRD patterns of $Sm(Fe_{0.95-x}Co_xNi_{0.05})_{12}$-B ($x$ = 0 ~ 0.5, B = 0 ~ 8%) thin films obtained from an in-plane configuration (various χ and φ angles) are shown in Fig. 4. As shown in Fig. 4(a), the (121), (031), (022), and (222) peaks from the 1:12 phase were clearly observed in the $Sm(Fe_{0.95}Ni_{0.05})_{12}$ thin film without B addition. Similar to the results in Fig. 3(a), it was confirmed that the intensity of peaks from the 1:12 phase decreased with the addition of B, and its intensity was restored by increasing the amount of Co substitution. When increasing the Co substitution amount x, (132) and (332) superlattice reflections were also observed, and the Co substitution amounts at which these peaks began to be observed were x = 0.4, 0.3, and 0.3 in the 0%B, 2%B, and 5%B samples, respectively. Furthermore, the peak intensities of the (132) and (332) peaks were stronger in the 2%B and 5%B samples compared with the sample without B addition. From the results shown so far, it was confirmed that increasing the amount of Co substitution and adding a small amount of B, such as 2%B or 5%B, promotes the formation of the Sm(Fe-Co-Ni)$_{12}$ phase.

Magnetization curves for $Sm(Fe_{0.95-x}Co_xNi_{0.05})_{12}$-B ($x$ = 0 ~ 0.5, B = 0 ~ 8%) thin films are shown in Fig. 5. As shown in Fig. 5(a), K_u of the B-free Sm(Fe-Co-Ni)$_{12}$ thin film decreased with increasing Co substitution amount x [(i)~(vi)], and it was confirmed that the easy axis of magnetization varied from perpendicular to the film plane to in-plane at x = 0.5. In addition, as shown in Fig. 5(b), by adding 2%B, the easy axis of magnetization of the Co-unsubstituted Sm(Fe-Ni)$_{12}$-B thin film was in the film plane. However, K_u increased as the amount of Co substitution increased up to x of 0.2 and decreased with further increase in x. When the B content was 5% (c), K_u similarly increased with Co substitution, reaching a maximum at x = 0.3. In contract, when B was added in larger amounts up to 8%, the easy axis of magnetization could not be obtained in the direction perpendicular to the film plane at any Co substitution amount x. Thus, it was confirmed that the addition of B to the Sm(Fe-Co-Ni)$_{12}$ thin film increases the Co substitution amount (x), which exhibits perpendicular magnetic anisotropy.

Scatter plots of the axial ratio c/a and the uniaxial magnetic anisotropy constant K_u for $Sm(Fe_{0.95-x}Co_xNi_{0.05})_{12}$-B ($x$ = 0 ~ 0.5, B = 0 ~ 8%) thin films are shown in Fig. 6. The value of c/a was obtained from the peak positions of the 1:12 phase in Figs. 3 and 4. For films without B, c/a increased as x increased up to 0.2 and then decreased with further increases in x. In the sample with 2% B addition, c/a decreased as x increased to 0.2, and at x = 0.3, c/a increased slightly, and a further increase in x resulted in a slight decrease in c/a. At 5%B, c/a decreased significantly with a Co substitution amount of x = 0.1, but it then increased at x = 0.2 and 0.3, and decreased slightly at 0.4. By adding 8%B, high c/a values were confirmed at x = 0.1 and 0.2, and these values decreased significantly with a further increase in B content. On the other hand, a high K_u value of 3.89 MJ/m^3 was obtained for the $SmFe_{12}$ thin

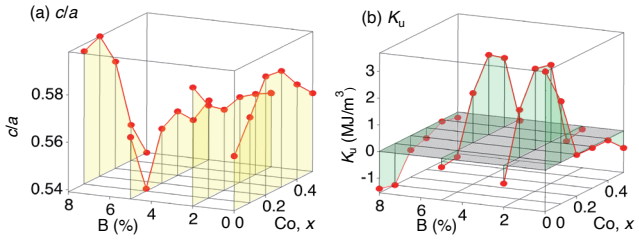

Fig. 6. Scatter plot of the axial ratio c/a and the uniaxial magnetic anisotropy constant K_u for $Sm(Fe_{0.95-x}Co_xNi_{0.05})_{12}$-B ($x = 0 \sim 0.5$, B = 0 ~ 8%) thin films.

film (x = 0, B = 0%) with no added B or Co. However, when the Co substitution amount x was 0.5, the K_u value dropped significantly and became negative. However, when 2% and 5% B were added, the K_u value increased with increasing Co substitution, and the easy axis of magnetization became perpendicular. In these B-added films, high K_u values were obtained at Co substitution amount x around 0.2 ~ 0.3. However, as the Co substitution amount x was further increased, K_u decreased. From these results, it was confirmed that positive values of K_u were obtained for films with contents of x = 0 to 0.1 (0%B), 0.1 to 0.3 (2%B), and 0.2 to 0.4 (5%B), and that the c/a values for samples in which the easy axis of magnetization was perpendicular to the film plane were in the range of 0.559 to 0.578. It was also confirmed that when the Co substitution amount was 0.2 ~ 0.5, c/a decreased while K_u increased with increasing the amount of B. Therefore, it is believed that adding B to $Sm(Fe\text{-}Co\text{-}Ni)_{12}$ thin film decreases the c/a and increases K_u. However, at 8% B, where the Co substitution amount was x = 0.4 ~ 0.5, the c/a decreased significantly, and K_u also exhibited low values. So, it is thought that the decrease in the c/a contributes to the reduction in K_u.

4. Conclusion

In this study, $Sm(Fe\text{-}Co)_{12}$ and $Sm(Fe\text{-}Co)_{12}$-B thin films with added Ni, which is expected to stabilize the $ThMn_{12}$-type phase without remarkable decreasing saturation magnetization, were prepared and the variation in the crystal structure and magnetic properties that result from variation of the film composition, such as the amount of Co and Ni substituted for Fe and the amount of B added were also investigated. It was found that the substitution of Co into Fe sites in $Sm(Fe_{1-x-y}Co_xNi_y)_{12}$ thin films elongates the lattice spacing of the c-plane, while the substitution of Ni inhibits the formation of the 1:12 phase and instead promotes the formation of Fe_5Ni and α-Fe phases. As the amount of Ni substitution increased, the easy axis of magnetization became predominantly in-plane, but by adding a small amount of B (2% and 5%) and substituting an optimal amount of Co, a composition region in which the easy axis of magnetization was perpendicular was obtained. In other words, it was found that the amount of Co substitution in the $Sm(Fe\text{-}Co\text{-}Ni)_{12}$-B thin film with perpendicular magnetic anisotropy increased with increasing B content. This research will provide valuable insight into the development of next-generation permanent magnets that exhibit high saturation magnetization when the Fe mole fraction is increased.

Acknowledgements This work was performed at the Research Institute for Engineering and Technology (High-Tech Research Center) at Tohoku Gakuin University. This work was partially supported by MEXT Program: Data Creation and Utilization-Type Material Research and Development Project (Digital Transformation Initiative Center for Magnetic Materials) Grant Number JPMXP1122715503.

References

1) Y. Hirayama, Y. K. Takahashi, S. Hirosawa, and K. Hono: *Scr. Mater.*, **138**, 62 (2017).
2) A. M. Gabay and G. C. Hadjipanayis: *Scr. Mater.*, **154**, 284 (2018).
3) P. Tozman, H. Sepehri-Amin, Y. K. Takahashi, and K. Hono: *Acta Mater.*, **153**, 354 (2018).
4) P. Tozman, Y. K. Takahashi, H. Sepehri-Amin, D. Ogawa, S. Hirosawa, and K. Hono: *Acta Mater.*, **178**, 114 (2019).
5) Y. K. Takahashi, H. Sepehri-Amin, and T. Ohkubo: *Adv. Mater.*, **22**, 449 (2021).
6) P. Tozman, H. Sepehri-Amin, and K. Hono: *Scr. Mater.*, **194**, 113686 (2021).
7) H. Sepehri-Amin, Y. Tamazawa, M. Kambayashi, G. Saito, Y. K. Takahashi D. Ogawa, T. Ohkubo, S. Hirosawa, M. Doi, T. Shima, and K. Hono: *Acta Mater.*, **194**, 337 (2020).
8) M. Kambayashi, H. Kato, Y. Mori, M. Doi, and T. Shima: *J. Magn. Soc. Jpn.*, **45**, 66 (2021).
9) A. Bolyachkin, H. Sepehri-Amin, M. Kanbayashi, Y. Mori, T. Ohkubo, Y. K. Takahashi, T. Shima, and K. Hono: *Acta Mater.*, **227**, 117716 (2022).
10) Y. Mori, S. Nakatsuka, S. Hatanaka, M. Doi, and T. Shima: *J. Magn. Soc. Jpn.*, **48**, 17 (2024).
11) H. Sepehri-Amin, N. Kulesh, Y. Mori, T. Ohkubo, K. Hono, and T. Shima: *Scr. Mater.*, **242**, 115955 (2024).
12) X. C. Kou, T. S. Zhao, R. Grössinger, H. R. Kirchmayr, X. Li, and F. R. de Boer: *Phys. Rev. B*, **47**, 3231 (1993).
13) M. Artigas, C. Piquer, J. Rubin, and J. Bartolome: *J. Magn. Magn. Mater.*, **196**, 653 (1999).
14) I. Dirba, J. Li, H. Sepehri-Amin, T. Ohkubo, T. Schrefl, and K. Hono: *J. Alloys Compd.*, **804**, 155 (2019).
15) A. Landa, P. Söderlind, E. E. Moore, and A. Perron: *Appl. Sci.*, **10**, 6037 (2020).
16) A. Landa, P. Söderlind, E. E. Moore, and A. Perron: *Metals*, **14**, 59 (2024).

Received Oct. 21, 2024; Revised Dec. 12, 2024; Accepted Jan. 17, 2025

J. Magn. Soc. Jpn., **49**, 32-36 (2025) <Paper>

Characteristics of PMSM with $Sm_2Fe_{17}N_3/Fe_{16}N_2$ Hybrid Bonded Magnets

İbrahim Çirozlar[1], Shunya Murakami[1], Kenji Nakamura[1], Tomoyuki Ogawa[1, 2], Shinpei Yamamoto[2, 3], Naoya Kobayashi[2], Hitoshi Yamamoto[2]

[1] Graduate School of Engineering, Tohoku University, *6-6-11 Aoba Aramaki Aoba-ku, Sendai 980-8579, Japan*

[2] Future Materialz Co. Ltd., *4-27-5 Zenpukuji Suginami-ku, Tokyo 167-0041, Japan*

[3] Sankei Giken Kogyo Co. Ltd., *2-5-1 Akabane-Minami Kita-ku, Tokyo 115-8555 Japan*

This paper presents an investigation into the performance of a surface-mounted permanent magnet synchronous motor (PMSM) utilizing $Sm_2Fe_{17}N_3/Fe_{16}N_2$ hybrid bonded magnets, developed as an alternative to traditional rare-earth-based magnets. The study aims to address the challenges associated with the high cost and supply chain vulnerabilities of rare-earth materials like neodymium and dysprosium. The motor's torque, efficiency, and losses under various loading conditions are evaluated by applying three-dimensional finite element method (3D-FEM) simulations and conducting experimental validation using a prototype motor. The experimental results closely align with the FEM simulations in terms of torque and efficiency, especially after a 40 mN·m load. However, discrepancies in iron losses are observed, with experimental values being approximately 2.5 W higher than FEM predictions. This variance is attributed to factors such as the rotor's overhang structure and the building factor of the motor core. Additionally, the study demonstrates that optimizing the magnet's properties could lead to a 32% increase in torque output. Future work will focus on improving magnet performance and refining FEM models for more practical applications.

Key words: $Sm_2Fe_{17}N_3/Fe_{16}N_2$ hybrid bonded magnet, Permanent magnet synchronous motor (PMSM), Three-dimensional finite element method (3D-FEM), Prototype test

1. Introduction

The relentless pursuit of energy efficiency and enhanced performance in electric motors has driven significant research into advanced materials and design optimizations. Among these motors, permanent magnet synchronous motors (PMSMs) are highly regarded for their superior power density, efficiency, and compactness, making them a key player in various industrial, automotive, and renewable energy applications. The growing demand for PMSMs is largely driven by their ability to deliver high torque and efficiency across a broad range of speeds. However, despite these advantages, the widespread adoption of PMSMs faces challenges due to their reliance on rare-earth magnets, particularly those containing neodymium (Nd) and dysprosium (Dy). Rare-earth elements are critical in producing high-performance magnets, but they come with inherent risks, such as fluctuating availability and rising costs, which stem from global supply chain vulnerabilities and geopolitical tensions. These issues have been highlighted by the Japanese Ministry of Economy, Trade, and Industry in their recent policy updates, where they emphasized the growing concern over supply chain instability for critical materials like rare-earths [1].

Moreover, extracting and processing rare-earth elements pose environmental challenges, contributing to the urgency for alternatives. As J.M.D. Coey discusses, the gap between the rising demand for permanent magnets and the finite supply of rare-earth elements, which has sparked intense research into alternative materials [2]. This has driven a global effort to explore more sustainable and cost-effective solutions without sacrificing motor performance. One such effort, the Element Strategy Initiative, focuses on reducing reliance on rare-earth magnets by advancing two primary approaches. The first approach aims to develop new rare-earth-free magnetic materials, while the second seeks to enhance the microstructure of existing rare-earth compounds, such as $Nd_2Fe_{14}B$ and $Sm_2Fe_{17}N_x$, to improve their performance while minimizing rare-earth content [3].

Based on the above initiative, this paper presents an investigation into the performance of a PMSM utilizing $Sm_2Fe_{17}N_3/Fe_{16}N_2$ hybrid bonded magnets, developed as an alternative to traditional rare-earth-based magnets. The motor's torque, efficiency, and losses are evaluated by applying three-dimensional finite element method (3D-FEM) simulations and conducting experimental validation using a prototype motor.

Corresponding author: İbrahim Çirozlar (e-mail: cirozlar.ibrahim.r2@dc.tohoku.ac.jp).

2. Specifications of Motor Characteristics

Prior to comparing the experimental results of the prototype motor with the findings of the finite element method (FEM) simulation, a series of preliminary tests were conducted. These tests aimed to characterize the magnetic properties of the $Sm_2Fe_{17}N_3/Fe_{16}N_2$ hybrid bonded magnet and to quantify the copper, iron, and mechanical losses inherent to the motor. Additionally, the current waveforms under various operating conditions were measured to provide accurate input data for the FEM analysis.

Fig. 1 presents the specifications of the surface-mounted PMSM employed in this study. The motor features a three-phase,

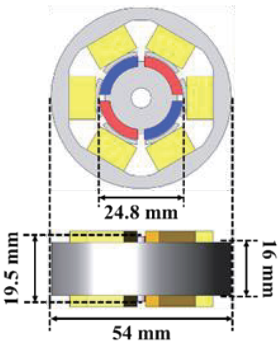

Winding method	Concentrated-winding
Rotor speed (rpm)	12600
Number of poles/slots	4/6
Diameter (mm)	54
Gap length (mm)	0.3
Material of iron core	35A300
Magnet length (mm)	3

Fig. 1 Specifications of the prototype surface-mounted PMSM.

four-pole, six-slot configuration with a concentrated winding arrangement. Notably, the motor exhibits an overhang structure, wherein the axial length of the rotor core exceeds that of the stator core. This design choice may influence the motor's performance characteristics, particularly with regard to iron loss.

The *B-H* loop of $Sm_2Fe_{17}N_3/Fe_{16}N_2$ hybrid bonded magnet, as determined through experimental measurements, is depicted in Fig. 2. The *B-H* curve reveals a coercive force (H_{cb}) of 280 kA/m and a residual magnetic flux density (B_r) of 0.53 T.

The structural configuration of the prototype motor is depicted in Fig. 3. The stator iron core is securely encased within the motor housing, providing both protection and mechanical stability. This design ensures the correct alignment between the stator and rotor, which is essential for achieving optimal electromagnetic interactions. Proper alignment plays a critical role in torque generation and operational efficiency, particularly at high rotational speeds.

Fig. 4 shows the experimental setup used to measure the no-load induced voltage. The experimental configuration consists of the prototype motor coupled to a drive motor using a rigid coupling. During the test, the drive motor maintains a constant rotational speed of 12,600 rpm. The induced voltage between the terminals of the prototype motor is measured using a precision scope coder.

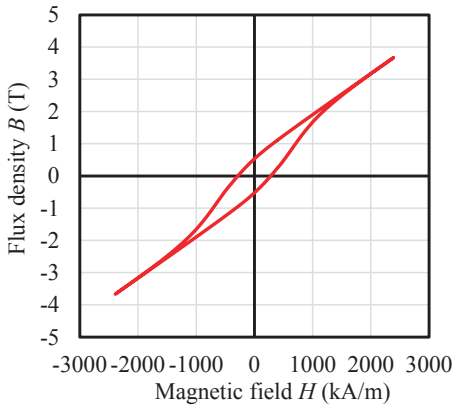

Fig. 2 Measured *B-H* loop of $Sm_2Fe_{17}N_3/Fe_{16}N_2$ hybrid bonded magnet.

Fig. 3 Appearance of the prototype surface-mounted PMSM (top) and its parts disassembled (bottom).

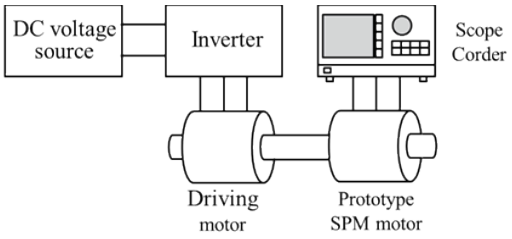

(a) Experimental configuration

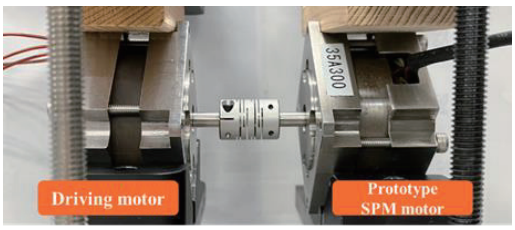

(b) Appearance of experimental setup

Fig. 4 Experimental configuration and its setup.

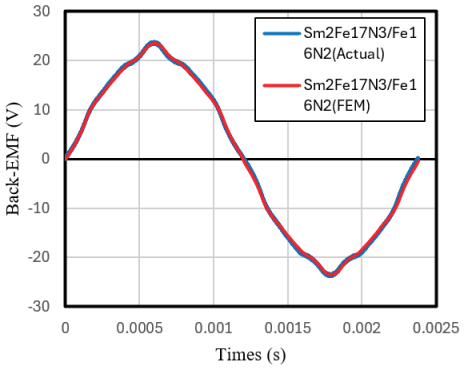

Fig. 5 Back-EMF waveform at no-load.

Fig. 5 illustrates the measured waveform of the no-load induced voltage. The measured no-load voltage was recorded at 15.7 V, corresponding to a magnetic flux linkage of approximately 20.6 mWb. The calculated values, obtained through Eq. (1) and (2) derived from fundamental electromagnetic principles.

$$V_{RMS} = \phi_{RMS} \cdot \omega \quad (1)$$

$$\psi_a = \sqrt{3} \cdot \phi_{RMS} \quad (2)$$

In conjunction with the no-load test, a mechanical loss test is conducted at various speeds. Prior to the test, the iron stator core of the prototype motor is replaced with a non-magnetic and non-conductive core of the same size. The prototype motor is then mechanically connected to the driving motor, which is operated at 12,600 rpm. Subsequently, the driving motor is run under no-load conditions. Accordingly, the mechanical loss of the prototype motor can be determined by calculating the difference between the input power with the mechanical connection ($P_{connected}$) and the input power without load (P_{NoLoad}), as shown in the following equation.

$$P_{Loss} = P_{connected} - P_{NoLoad} \quad (3)$$

Fig. 6 indicates the measured mechanical loss for different speeds, which is used to estimate the FEM-derived efficiency in the next chapter.

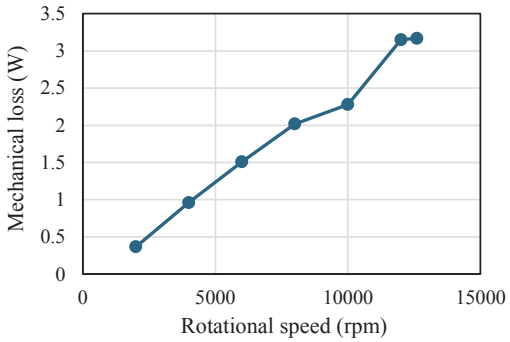

Fig. 6 Measured mechanical loss for different speeds.

Fig. 7 illustrates the experimental setup employed for the load tests. The prototype motor is driven at a constant speed of 12,600 rpm using a three-phase pulse-width modulation (PWM) inverter with sensorless vector control. A hysteresis brake is utilized to apply a controlled load to the motor. The motor's torque and rotational speed are measured using a motor analyzer, while winding current and input power are acquired via a power analyzer. The dc power supply voltage is maintained at 48 V.

The prototype motor is loaded incrementally from 0 mN·m to 220 mN·m (in steps of 20 mN·m) while rotating at a constant speed of 12,600 rpm (420 Hz). The corresponding current waveforms are measured, and Fig. 8 shows the measured current waveforms of U-phase for one period cycle for 20 mN·m, 80 mN·m, and 200 mN·m loadings. These waveforms are subsequently used as inputs for the 3D-FEM analysis to ensure an accurate representation of the motor's behavior under load.

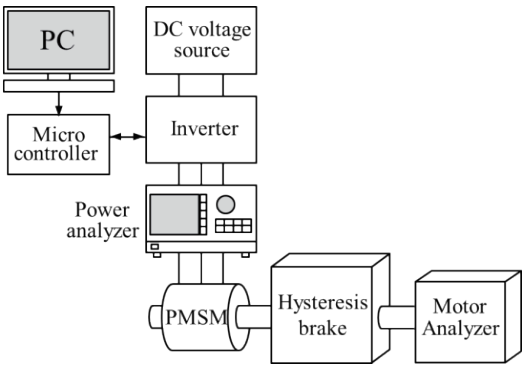

(a) Experimental configuration

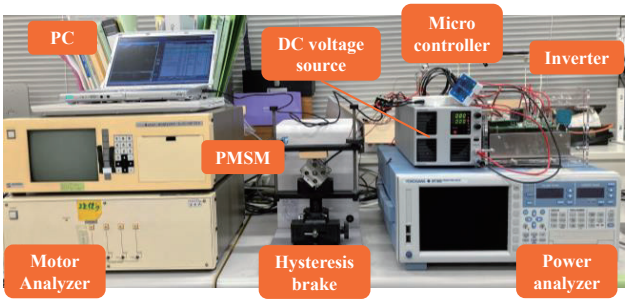

(b) Appearance of the experimental setup

Fig. 7 Experimental setup for the load tests.

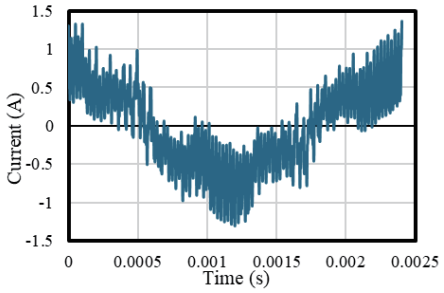

(a) 20 mN·m

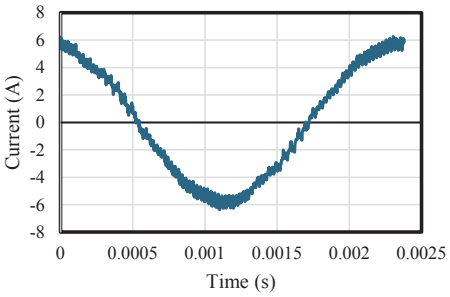

(b) 80 mN·m

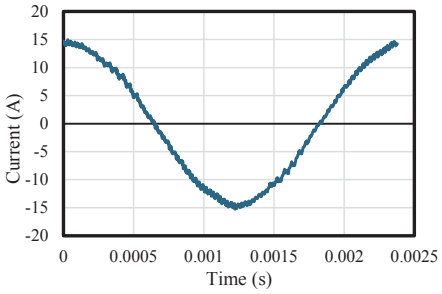

(c) 200 mN·m

Fig. 8 Measured current waveforms used as inputs for 3D-FEM.

3. 3D-FEM Design and Result Comparisons

The PMSM prototype was modeled in FEM, reflecting the 1/4 of the same three-phase, four-pole, six-slot motor with concentrated windings, as shown in Fig. 9. The mesh design consisted of 95,381 elements, and JMAG-Designer Ver. 23.1 of JSOL Co., Ltd. was used for the 3D-FEM simulation. The measured current waveforms shown in Fig. 8 were inputted into the simulation, ensuring that the motor speed and current phase angle matched the experimental conditions.

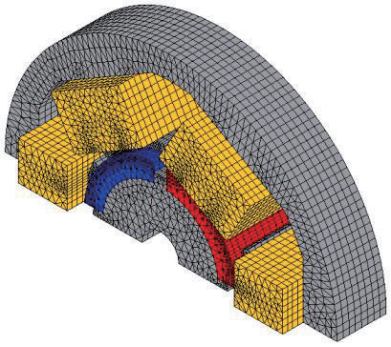

Fig. 9 3D-FEM model of the prototype surface-mounted PMSM.

Fig. 10 illustrates the comparison of measured and calculated torque versus current density characteristics. Both the experimental tests and FEM simulations demonstrate excellent alignment, with any differences being too minor to significantly impact the results. This near-perfect correlation validates the accuracy of the FEM model in replicating the motor's torque response under varying current densities.

Fig. 11 shows the torque versus efficiency characteristics. The experimental efficiency values were calculated using the motor's input power (P_{in}) and output power (P_{out}), as defined in the following equation.

$$\eta_{meas} = \frac{P_{out}}{P_{in}} \times 100\ (\%) \tag{4}$$

In contrast, the FEM-derived efficiency was determined by incorporating the machine's output power (P_{out}), copper losses (W_c), iron losses (W_i), and mechanical losses (W_m), as shown in the following equation.

$$\eta_{fem} = \frac{P_{out}}{P_{out}+W_c+W_i+W_m} \times 100\ (\%) \tag{5}$$

The copper loss was calculated using $r \cdot i^2$ where r is the winding resistance and i is the winding current. The iron loss was estimated based on Steinmetz's experimental equation, derived from the flux density distribution obtained via FEM. The mechanical loss was given by the measured values shown in Fig. 6. From the figure, it can be observed that the maximum measured efficiency of the prototype motor was around 89.3% at 160 mN·m of torque, while the calculated efficiency peaked at 90.8% at 120 mN·m.

Fig. 12 shows the comparison of measured and calculated losses. In this experimental system, since the iron loss W_i cannot

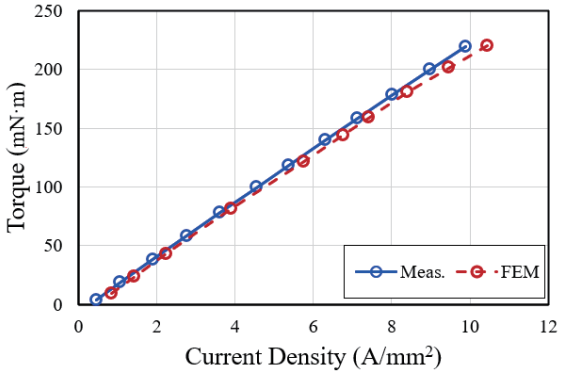

Fig. 10 Comparison of measured and calculated torque versus current density characteristics.

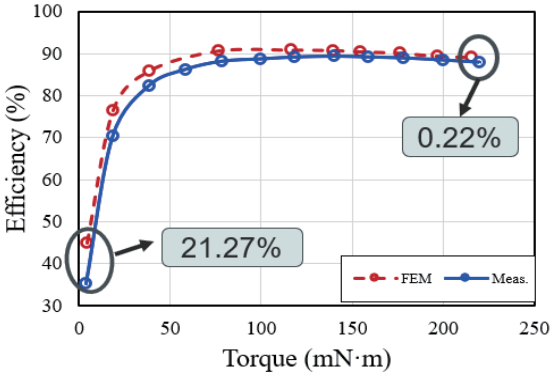

Fig. 11 Comparison of measured and calculated efficiencies.

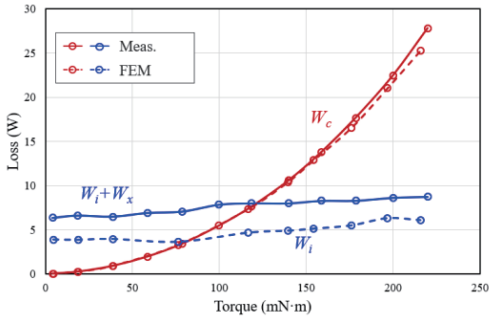

Fig. 12 Comparison of measured and calculated losses.

be measured directly, the sum of the iron loss and other losses ($W_i + W_x$) was obtained by subtracting the mechanical output and copper loss from the input power and the mechanical loss, shown in Fig. 6, as shown in Eq. (6).

$$W_i + W_x = P_{in} - P_{out} - W_c - W_m \tag{6}$$

The copper losses obtained from both FEM simulations and prototype testing align closely. However, the iron losses measured during testing are about 2.5 W higher than those predicted by the FEM. This discrepancy could be attributed to the rotor's overhang structure and the building factor of the motor core.

4. Motor performance with the latest hybrid bounded magnet

In previous chapters, the surface-mounted PMSM employing $Sm_2Fe_{17}N_3/Fe_{16}N_2$ hybrid bonded magnets have been prototyped and tested. The experimental results closely matched the FEM simulations. While there was a minor iron loss discrepancy, the motor's overall performance, the overall performance of the motor was satisfactory and aligned with the intended design goals.

Now, the performance improvement of the hybrid bonded magnet is in progress. Fig. 13 shows the latest *B-H* loop of $Sm_2Fe_{17}N_3/Fe_{16}N_2$ hybrid bonded magnet. It has a coercive force (H_{cb}) of 380 kA/m and a residual magnetic flux density (B_r) of 0.71 T, which are almost competitive with those of the Nd-Fe-B bonded magnet in Ref. 4) (H_{cb}: 460 kA/m, B_r: 0.74 T).

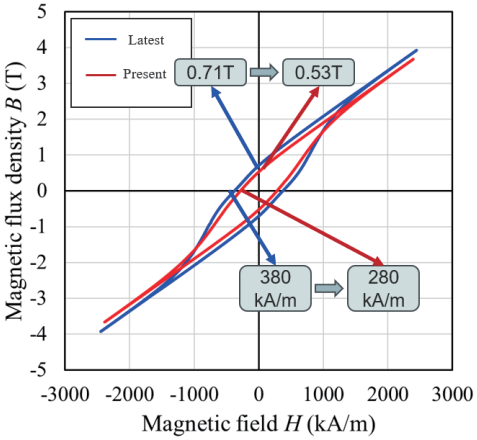

Fig. 13 Present and latest *B-H* loops of $Sm_2Fe_{17}N_3/Fe_{16}N_2$ hybrid bonded magnets.

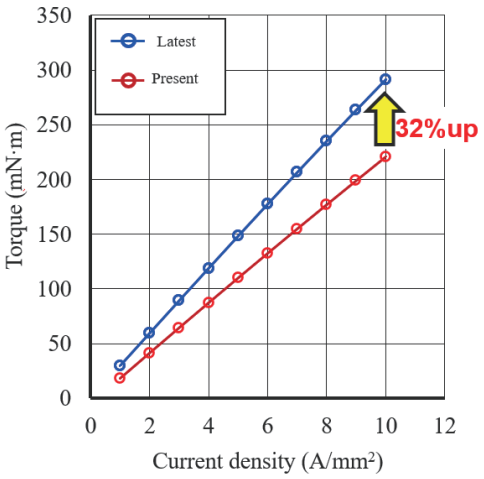

Fig. 14 Comparison of the calculated torque versus current density characteristics using the present and latest hybrid bonded magnets.

Fig. 14 illustrates the calculated torque versus current density characteristics using the present and latest hybrid bonded magnets shown in Fig. 13. The figure highlights that the torque output could increase by up to 32% with the latest magnet characteristics. The next step of this study is to prototype the PMSM with the latest hybrid bonded magnets and carry out the experiments.

5. Conclusion

In conclusion, the surface-mounted PMSM employing $Sm_2Fe_{17}N_3/Fe_{16}N_2$ hybrid bonded magnets was prototyped and tested. The experimental results closely matched the FEM simulations, confirming the validity of the hybrid magnet's application in PMSM designs. Although there was a minor iron loss discrepancy, the motor's overall performance of the motor—both in terms of torque and efficiency—was satisfactory and aligned with the intended goals.

Furthermore, the latest characteristic of the $Sm_2Fe_{17}N_3/Fe_{16}N_2$ hybrid bonded magnet was indicated, showing a coercive force of 380 kA/m and a residual magnetic flux density of 0.71 T, which are almost competitive with those of the Nd-Fe-B bonded magnet. The motor's torque with the latest hybrid bonded magnets could be increased by 32%.

The success of this study opens up new avenues for the development of motors that are less reliant on rare-earth materials, contributing to more sustainable and cost-effective motor designs.

Acknowledgement This study was supported by WISE Program for AI electronics in Tohoku University.

References

1) Ministry of Economy, Trade and Industry, Japan: "Policy for ensuring stable supply of permanent magnets", p. 208 (2024) (https://www.meti.go.jp/english/report/data/wp2023/pdf/2-1-2.pdf).
2) J. M. D. Coey: *Scr. Mater.*, **67**, 524 (2012).
3) K. Hono and S. Hirosawa: *Magune (Magn. Jpn.)*, **7**, 290 (2012) (in Japanese).
4) Y. Uchiyama, K. Nakamura, O. Ichinokura, H. Goto, and H.J. Guo: *Trans. Magn. Soc. Jpn. (Special Issues)*, **4**, 67 (2020) (in Japanese).

Received Oct. 21, 2024; Accepted Dec. 10, 2024

Editorial Committee Members・Paper Committee Members

Notice for Photocopying

編集委員・論文委員

複写をされる方へ

Journal of the Magnetics Society of Japan

Vol. 49 No. 2 (通巻第338号) 2025年3月1日発行

Vol. 49 No. 2 Published Mar. 1, 2025
by the Magnetics Society of Japan
Tokyo YWCA building Rm207, 1–8–11 Kanda surugadai, Chiyoda-ku, Tokyo 101–0062
Tel. +81–3–5281–0106 Fax. +81–3–5281–0107

Printed by JPC Co., Ltd.
Sports Plaza building 401, 2–4–3, Shinkamata Ota-ku, Tokyo 144–0054
Advertising agency: Kagaku Gijutsu-sha

発行：(公社)日本磁気学会 101–0062 東京都千代田区神田駿河台 1–8–11 東京YWCA会館 207 号室
製作：ジェイピーシー 144–0054 東京都大田区新蒲田 2–4–3 スポーツプラザビル401 Tel.（03）6715–7915
広告取扱い：科学技術社 111–0052 東京都台東区柳橋 2–10–8 武田ビル 4F Tel.（03）5809–1132